

1
2 **Facile fabrication of ultrathin freestanding nanoporous Cu and Cu-Ag films with high SERS**
3 **sensitivity by dealloying Mg-Cu(Ag)-Gd metallic glasses**
4
5

6 Yuan-Yun Zhao^{1,2}, Feng Qian⁴, Chengliang Zhao¹, Chunxiao Xie¹, Jianguo Wang¹,
7 Chuntao Chang^{1,*}, Yanjun Li^{2,*}, Lai-Chang Zhang^{3,*}
8
9

10 ¹*Neutron Scattering Technical Engineering Research Center, School of Mechanical Engineering, Dongguan University*
11 *of Technology, Dongguan 523808, China*

12 ²*Department of Materials Science and Engineering, Norwegian University of Science and Technology, Trondheim*
13 *7491, Norway*

14 ³*Edith Cowan University, School of Engineering, 270 Joondalup Drive, Joondalup, Perth, WA 6027, Australia*

15 ⁴*School of Materials Science and Engineering, Beijing Institute of Technology, 100081, Beijing, China*
16
17

18
19 **Abstract**
20

21
22 Nanoporous metals prepared by dealloying have attracted increasing attention due to their
23 interesting size-dependent physical, chemical, and biological properties. However, facile fabrication
24 of metallic ultrathin freestanding nanoporous films (UF-NPFs) by dealloying is still challenging.
25 Herein, we report a novel strategy of facile preparation of flexible Cu, Cu₃Ag, and CuAg UF-NPFs
26 by dealloying thick Mg-Cu(Ag)-Gd metallic glass ribbons. During dealloying, the local reaction
27 latent heat-induced glass transition of the precursor ribbons leads to the formation of a solid/liquid
28 interface between the initially dealloyed nanoporous layer and the underlying supercooled liquid
29 layer. Due to the bulging effect of in situ generated H₂ on the solid/liquid interface, Cu, Cu₃Ag, and
30 CuAg UF-NPFs with thicknesses of ~200 nm can self-peel off from the outer surface of the
31 dealloying ribbons. Moreover, it was found that the surface-enhanced Raman scattering (SERS)
32 detection limit of Rhodamine 6G (R6G) on the Cu and CuAg UF-NPF substrates are 10⁻⁶ M and 10<sup>-
33 11</sup> M, respectively, which are lower than most of the Cu and Cu-Ag substrates prepared by other
34 methods. This work presents a reliable simple strategy to synthesize a variety of cost effective and
35 flexible metallic UF-NPFs for functional applications.
36
37
38
39
40
41
42
43
44
45
46
47

48 **Keywords**

49 Metallic glasses; Dealloying; Nanoporous metals; Ultrathin freestanding films; Surface-enhanced
50 Raman scattering (SERS)
51
52
53
54

55 *Corresponding authors.

56
57 Email address: changct@dgut.edu.cn (C. Chang), yanjun.li@ntnu.no (Y. Li),
58 lc Zhangimr@gmail.com (L.-C. Zhang).
59
60

1. Introduction

Nanoporous metals have attracted extensive attention due to their intriguing physical, chemical, and mechanical properties, which give rise to a wide range of potential applications in catalysts, sensors, supercapacitors, surface-enhanced Raman scattering (SERS)-active substrates, and so on [1-5]. During the past decades, numerous strategies have been proposed to synthesize a variety of nanoporous metals, including template methods [1-2,6], dealloying [7-8], galvanic replacement reactions [9], and electrochemical deposition [10-11]. Among these methods, the dealloying method has become one of the most efficient ways to fabricate nanoporous metals [3-8]. During dealloying, as the less noble metal is selectively removed from the precursor alloy, the more noble metal atoms diffuse and reorganize into a well-defined three-dimensional bi-continuous porous structure with nanoscale ligaments/pores [7]. To date, many nanoporous metals (e.g., Au, Pt, Pd, Ag, Cu, CuAg, PtFe) have been prepared by dealloying various crystalline precursor alloys [3-4,6-7,12-13] or metallic glass precursor alloys [5,14-18]. In recent decades, as a special type of nanoporous metals, metallic ultrathin freestanding nanoporous films (UF-NPFs) have attracted increasing attention due to their unique structures, properties, and considerable potential for a broad range of applications, such as separation membranes, sensors, flexible SERS substrates, and catalysts [19-24]. However, because nanoporous metals prepared by the dealloying approach usually maintain the thickness and shape as of the corresponding precursor alloys [12,25], the primary challenge in preparing metallic UF-NPFs by dealloying is the preparation of ultrathin freestanding precursor alloy films. Generally, the simplest and most direct way to prepare ultrathin freestanding precursor alloy films is continuous rolling. For example, an Au-Ag alloy sample with superplasticity can be hammer-rolled into ultrathin freestanding Au-Ag alloy film with a thickness of 100-200 nm. Thus, Au UF-NPFs (100-200 nm in thickness) can be easily prepared by dealloying ultrathin freestanding Au-Ag alloy films [7,19]. However, such a superplastic characteristic is only demonstrated in very few alloy systems, and most precursor alloys used for dealloying usually contain brittle intermetallic compounds, which cannot be rolled into ultrathin freestanding precursor alloy films. For example,

1
2 to prepare nanoporous Cu or Ag by dealloying, the less noble elements in the precursor alloys
3
4 mainly include Mg, Zn, Al, and Mn, resulting in the formation of brittle intermetallic compounds
5
6 (such as Mg₂Cu and Zn₃Ag) in the precursor alloys [12-13, 26-27]. Thus, it is unrealistic to prepare
7
8 Cu or Ag UF-NPFs by dealloying rolled ultrathin freestanding precursor alloy films. An alternative
9
10 approach to prepare precursor alloy films is melt spinning. However, the minimum thickness of the
11
12 alloy films prepared by melt spinning is usually greater than 10 μm. Therefore, the preparation of
13
14 metallic UF-NPFs by ordinary dealloying approach remains a great challenge.
15
16

17
18 SERS, featured with superior surface sensitivity and specificity, has become a very powerful
19
20 technique in several sensing fields, such as detection of pollutants in water, air and soil [28,29]; in
21
22 vivo drug tracking [30]; and in situ monitoring of chemical reactions [31]. In addition to the high
23
24 sensitivity of analyses, the recently practical implementation of SERS substrates for real in-situ
25
26 analyses requires the introduction of flexible SERS substrates for express, outdoors measurements
27
28 [32]. Compared with conventional rigid substrates (e.g., silicon, glass), flexible substrates can be
29
30 wrapped onto curved surfaces for in situ detection and can easily be cut into arbitrary shapes and
31
32 sizes [33]. Generally, flexible SERS substrates can be prepared by the assembly of metal
33
34 nanoparticles on flexible substrates [22,34], deposition of metal nanoparticles on the surfaces of
35
36 polymer thin films [32,35], embedding of metal nanostructures in fiber arrays, and using template-
37
38 assisted techniques [36-38]. However, most these methods are complex and require multiple steps.
39
40
41
42
43

44
45 In this work, we present a novel dealloying strategy on facile preparation of flexible Cu and
46
47 Cu-Ag (Cu₃Ag and CuAg) UF-NPFs by dealloying thick Mg-Cu(Ag)-Gd metallic glass ribbons
48
49 with low glass transition temperature ($T_g < 150^\circ\text{C}$). The phase constitution, morphology, and element
50
51 distribution of the as-prepared Cu, Cu₃Ag, and CuAg UF-NPFs were investigated in detail. The
52
53 formation mechanism of the as-prepared Cu, Cu₃Ag, and CuAg UF-NPFs was revealed by
54
55 investigating the morphology and composition of the sequential intermediates sampled at different
56
57 reaction times. Moreover, the SERS performance of the as-prepared Cu, Cu₃Ag, and CuAg UF-NPF
58
59 substrates was investigated and discussed.
60

2. Experimental

$Mg_{61}Cu_{28}Gd_{11}$, $Mg_{61}Cu_{21}Ag_7Gd_{11}$, and $Mg_{61}Cu_{14}Ag_{14}Gd_{11}$ (at. %) alloy ingots were prepared by induction melting mixtures of pure Mg (>99.95 wt.%), Cu (>99.95 wt.%), Ag and Gd (>99.9 wt.%) metals in an argon atmosphere. $Mg_{61}Cu_{28}Gd_{11}$, $Mg_{61}Cu_{21}Ag_7Gd_{11}$, and $Mg_{61}Cu_{14}Ag_{14}Gd_{11}$ metallic glass ribbons with widths of 3-5 mm and thicknesses of 150-200 μm were prepared by a single copper roller melt-spinning process. The Cu, Cu_3Ag , and CuAg UF-NPFs were prepared by simply dipping $Mg_{61}Cu_{28}Gd_{11}$, $Mg_{61}Cu_{21}Ag_7Gd_{11}$, and $Mg_{61}Cu_{14}Ag_{14}Gd_{11}$ metallic glass ribbons into dilute HCl/ethanol solution for 25 min, 120 min, and 120 min, respectively. The volume ratio of 12 mol L⁻¹ HCl aqueous solution to ethanol was 1:200, 1:500, and 1:500, respectively. Then the dealloyed Cu and Cu-Ag UF-NPFs were rinsed with ethanol repeatedly.

The morphologies of the intermediate products and the as-prepared Cu, Cu_3Ag , and CuAg UF-NPFs were characterized by scanning electron microscopy (SEM) equipped with energy dispersive X-ray spectroscopy (EDS). Transmission electron microscopy (TEM), high resolution transmission electron microscopy (HRTEM), selected area electron diffraction (SAED), energy-dispersive X-ray spectroscopy (EDS), scanning transmission electron microscopy (STEM), and element distribution spectral maps were obtained by a JEOL 2100F. The crystal structures of the as-prepared samples were examined using a Bruker D8 Advance X-ray diffractometer (XRD) with a Cu K_{α} radiation ($\lambda=0.1542$ nm) source. The glass transition temperature of the precursor alloys was investigated by differential scanning calorimetry (DSC) at a heating rate of 20 K min⁻¹.

The surface-enhanced Raman spectra of Cu, Cu_3Ag , and CuAg UF-NPFs were acquired by using a dispersive Raman microscope operated with a 532 nm laser. Rhodamine 6G (R6G) was used as the probe molecule, which was dissolved into ethanol with a concentration of 10⁻⁴ M~10⁻¹² M. The UF-NPF substrates were immersed in the solutions for 1 h for sufficient molecule adsorption before SERS measurements.

3. Results and Discussion

3.1. Preparation and characterization of the Cu, Cu_3Ag , and CuAg UF-NPFs

1
2 Mg-Cu(Ag)-Gd metallic glass ($Mg_{61}Cu_{28}Gd_{11}$, $Mg_{61}Cu_{21}Ag_7Gd_{11}$, and $Mg_{61}Cu_{14}Ag_{14}Gd_{11}$)
3
4 ribbons with thicknesses of 150-200 μm were used as precursor alloys for the preparation of Cu,
5
6 Cu_3Ag , and CuAg UF-NPFs, respectively. Dilute HCl/ethanol solutions with volume ratios of 12
7
8 mol L⁻¹ HCl aqueous solution to ethanol of 1:200, 1:500, and 1:500 were used as the erosion
9
10 solution for the synthesis of Cu, Cu_3Ag , and CuAg UF-NPFs, respectively. Fig. 1a shows the
11
12 photographs of a typical synthetic procedure of Cu UF-NPF by dealloying a $Mg_{61}Cu_{28}Gd_{11}$ metallic
13
14 glass ribbon for different times. After dealloying for 1 min, the appearance of a few visible bubbles
15
16 indicates that the reaction speed is very slow in such a dilute HCl/ethanol solution. Unlike
17
18 conventional dealloying reactions, in which the nanoporous metals maintain the thickness and shape
19
20 of the corresponding precursor alloys, an initial separation of the intermediate Cu UF-NPFs from
21
22 the dealloyed ribbon can be observed after dealloying for 8 min. After dealloying for 25 min, fully
23
24 dealloyed Cu UF-NPFs with perfect Cu metallic luster self-peel off from the outer surface of the
25
26 thick $Mg_{61}Cu_{28}Gd_{11}$ metallic glass ribbon. Through similar dealloying processes, Cu_3Ag and CuAg
27
28 UF-NPFs can also be prepared by dealloying the outer surface of $Mg_{61}Cu_{21}Ag_7Gd_{11}$ and
29
30 $Mg_{61}Cu_{14}Ag_{14}Gd_{11}$ metallic glass ribbons, respectively (Fig. 1b-c). It is worth noting that there is a
31
32 slight difference between the self-peeling processes of Cu UF-NPFs and Cu-Ag UF-NPFs. Due to a
33
34 possible local residual stress on the sides of the dealloyed $Mg_{61}Cu_{28}Gd_{11}$ metallic glass ribbon, the
35
36 initial formed intermediate Cu UF-NPF tended to break in there (Fig. 1a, after dealloying for 15
37
38 min). Thus, two pieces of Cu UF-NPFs self-peeled off from the upper and lower surfaces of the
39
40 $Mg_{61}Cu_{28}Gd_{11}$ metallic glass ribbon (another piece of the Cu UF-NPF was blocked by the 90-
41
42 degree-rotated remaining metallic glass ribbon, as shown in Fig. 1a). For the Cu_3Ag and CuAg UF-
43
44 NPFs, which were prepared in a more diluted HCl/ethanol solution, although they have completely
45
46 separated from the remaining $Mg_{61}Cu_{21}Ag_7Gd_{11}$ and $Mg_{61}Cu_{14}Ag_{14}Gd_{11}$ metallic glass ribbons after
47
48 dealloying for 120 min, the remaining ribbons were completely enclosed within the capsule shell-
49
50 like Cu-Ag UF-NPFs. Fig. 1b and c show that the remaining $Mg_{61}Cu_{21}Ag_7Gd_{11}$ metallic glass
51
52 ribbon can be removed by tearing off the capsule shell-like Cu_3Ag UF-NPF. This phenomenon
53
54
55
56
57
58
59
60

1 demonstrates that the as-prepared Cu₃Ag UF-NPFs are very ductile and flexible. Fig. 1d-f shows
2 representative low-magnification SEM images of the as-prepared Cu, Cu₃Ag, and CuAg UF-NPFs,
3 which are uniform and almost crack-free across the entire specimens, and can be easily bent like
4 flexible clothes. The high-magnification SEM images (Fig. 1g-i) demonstrate that the as-prepared
5 Cu, Cu₃Ag, and CuAg UF-NPFs have thicknesses of 210±10 nm, 185±10 nm, and 180±10 nm,
6 respectively. The average ligament size in the Cu, Cu₃Ag, and CuAg UF-NPFs was determined as
7 ~25 nm, ~30 nm, and ~35 nm, respectively. The average compositions of the Cu, Cu₃Ag, and CuAg
8 UF-NPFs were determined as Cu, Cu₇₇Ag₂₃, and Cu₅₂Ag₄₈, respectively. These results are well
9 consistent with our design, in which the molar ratios of Cu:Ag in the Mg₆₁Cu₂₁Ag₇Gd₁₁ and
10 Mg₆₁Cu₁₄Ag₁₄Gd₁₁ metallic glass precursor alloys are 3:1 and 1:1, respectively.
11
12
13
14
15
16
17
18
19
20
21
22
23
24
25

26 Fig. 2 shows the XRD patterns of the Mg-Cu(Ag)-Gd metallic glass precursor ribbons and the
27 as-prepared Cu, Cu₃Ag, and CuAg UF-NPFs. Only a broad diffraction maximum without any
28 detectable crystalline peaks can be observed on each XRD pattern of the Mg-Cu(Ag)-Gd metallic
29 glass ribbons, demonstrating their homogeneous amorphous structure [39,40]. All of the diffraction
30 peaks of the Cu UF-NPFs can be indexed to the face-centered cubic (fcc) Cu phase. The XRD
31 pattern of the Cu₃Ag UF-NPFs consists of overlapping diffraction peaks attributed to both the fcc
32 Cu and Ag phases. Upon increasing the Ag content, the CuAg UF-NPFs mainly consist of a single
33 fcc Ag phase (and with trace amount of fcc Cu phase as well) without any shift of the diffraction
34 angles of Ag lattice. This phenomenon is very interesting, because the phase constitution of the
35 CuAg UF-NPFs prepared by the present dealloying approach is completely different from that of
36 the eutectic Cu₅₀Ag₅₀ alloy prepared by melt solidification, which consists of almost equivalent
37 amount of immiscible fcc Cu and fcc Ag phases [41]. Moreover, based on Vegard's law, there is a
38 linear relation between the crystal lattice parameter of an alloy and the concentrations of the
39 constituent elements [42]. However, herein the CuAg UF-NPFs just consist of a single fcc Ag phase
40 without any shift of the diffraction angles of the Ag lattice, indicating the formation of a
41 supersaturated fcc Ag(Cu) solid solution. This phenomenon is not isolated. For example, a
42
43
44
45
46
47
48
49
50
51
52
53
54
55
56
57
58
59
60

1
2 nonequilibrium synthetic strategy to overcome the immiscibility of Cu-based bimetallic
3
4 nanoparticles was just reported [43]. Similar phenomena have also been reported for chemical
5
6 synthesis of bimetallic Ag-Ni alloy nanoparticles, in which the solution of Ni into the
7
8 supersaturated Ag phase does not lead to the shift of the diffraction angles of the Ag lattice [44,45],
9
10 although Ag and Ni are immiscible based on the Ag-Ni phase diagram [41].
11
12

13
14 Fig. 3a-c show TEM images of the ligaments in Cu, Cu₃Ag, and CuAg UF-NPFs, respectively.
15
16 The average ligament sizes are determined as ~24 nm, ~28 nm, and ~35 nm, respectively, which are
17
18 well consistent with the results shown in the corresponding SEM images. The high-magnification
19
20 TEM images of the ligaments show that the Cu and CuAg UF-NPFs consist of single Cu and Ag
21
22 phases with (111) lattice spacings of 0.208 nm and 0.236 nm, respectively (Fig. 3d-f). The Cu₃Ag
23
24 UF-NPF consists of both Cu phase with a (111) lattice spacing of 0.208 nm and Ag phase with a
25
26 (111) lattice spacing of 0.237 nm (Fig. 3e). These results are well consistent with the XRD results
27
28 (Fig. 2) and the SAED patterns of the Cu, Cu₃Ag, and CuAg UF-NPFs (Fig. 3g-i). The elemental
29
30 distributions of Cu and Ag in Cu₃Ag and CuAg UF-NPFs were further investigated by STEM
31
32 coupled with EDS. Although Cu and Ag are distributed throughout the ligaments in the Cu₃Ag UF-
33
34 NPF, their distribution are inhomogeneous (Fig. 4a-d). Specifically, here a Cu-rich (or Ag-poor)
35
36 area is evident in the labeled region *A* (Fig. 4c-d). The high-magnification TEM image of region *A*
37
38 further confirms that such a Cu-rich area is associated with the presence of fcc Cu(Ag) phase with a
39
40 (111) lattice spacing of 0.208 nm (Fig. 4e-f). In the adjacent Ag-rich area (labeled as region *B*), a
41
42 fcc Ag(Cu) phase with a (111) lattice spacing of 0.236 nm is observed (Fig. 4e, g). These results
43
44 demonstrate that the Cu₃Ag UF-NPFs are not composed of separate fcc Cu and fcc Ag phases, but
45
46 consist of both Cu-rich fcc Cu(Ag) phase with Ag as a solute and Ag-rich fcc Ag(Cu) phase with
47
48 Cu as a solute. For the CuAg UF-NPFs, Fig. 4h-k shows a high degree of homogeneity and
49
50 essentially a uniform distribution of solute Cu in a supersaturated fcc Ag(Cu) solid solution.
51
52
53
54
55
56
57

58 *3.2. Formation mechanism*

59
60

1
2 To investigate the formation mechanism of Cu and Cu-Ag UF-NPFs by the present dealloying
3
4 approach, the morphology and composition of two sequential intermediate products (sampled at
5
6 reaction times of 3 min and 6 min) by dealloying $Mg_{61}Cu_{28}Gd_{11}$ metallic glass ribbon were
7
8 investigated (Fig. 5). The original outer surface of the $Mg_{61}Cu_{28}Gd_{11}$ metallic glass ribbon prepared
9
10 by melt spinning is almost an ideal smooth surface (Fig. 5a). After dealloying for 3 min, the
11
12 dealloyed ribbon consists of three different layers along the depth direction: layer *I*- rudimentary
13
14 nanoporous Cu layer (Fig. 5c), layer *II*- local “melted” layer, and layer *III*- unreacted metallic glass
15
16 ribbon (Fig. 5c-d). Because the glass transition temperature (T_g) of the Mg-Cu(Ag)-Gd metallic
17
18 glasses is as low as 143-149 °C (Fig. 5b), the reaction latent heat-induced local temperature can
19
20 easily increase up to T_g ; thus, glass-transition-induced local “melting” (phase transformation from
21
22 solid glassy phase to supercooled liquid phase) of the precursor ribbon occurred underlying the
23
24 rudimentary nanoporous Cu layer. Fig. 5d demonstrates the cracked-mud-like “melted” layer with a
25
26 thickness of $\sim 6 \mu m$ and one of the gas (in situ-generated H_2) escaped site within it (region A in Fig.
27
28 5d). The average compositions of the rudimentary nanoporous Cu layer, the local “melted” layer,
29
30 and the remained ribbon at 3 min were determined as $Mg_{21}Cl_1Cu_{70}Gd_8$, $Mg_{59}Cl_5Cu_{26}Gd_{10}$, and
31
32 $Mg_{59}Cu_{29}Gd_{12}$, respectively. These results indicate that the erosion speed of Mg and Gd during the
33
34 first 3 min is very fast, but considerable amounts of Mg and Gd remain in the rudimentary
35
36 nanoporous Cu layer. In addition, a considerable amount of Cl (5 at.%) in the local “melted” layer
37
38 implies that HCl has been mixed with it and some of the as-formed $MgCl_2$ and $GdCl_3$ are retained in
39
40 it. After dealloying for 6 min, the flexible Cu-rich UF-NPF with a composition of
41
42 $Mg_5Cl_{0.5}Cu_{93}Gd_{1.5}$ is initially separated from the outer surface of $Mg_{61}Cu_{28}Gd_{11}$ metallic glass
43
44 ribbon, while part of the previous “melted” layer is dealloyed into intermediate nanoporous Cu (Fig.
45
46 5e-f). As the dealloying reaction proceeds, the residual Mg and Gd in the brownish-black Cu-rich
47
48 UF-NPF would completely dissolve, and finally Cu UF-NPF with perfect Cu metallic luster would
49
50 self-peel off from the metallic glass ribbon (Fig. 1a).
51
52
53
54
55
56
57
58
59
60

1
2 The formation mechanism of Cu and Cu-Ag UF-NPFs is schematically illustrated in Fig. 6.
3
4 During the first stage of dealloying, the dissolution of the less noble Mg and Gd on the outer surface
5
6 of the precursor ribbon leads to the formation of a thin layer of rudimentary nanoporous Cu or Cu-
7
8 Ag with considerable amount of residual Mg and Gd (Fig. 6a). As the reaction proceeds, the
9
10 thickness of the rudimentary nanoporous Cu or Cu-Ag layer gradually increases, which hinders the
11
12 latent heat transfer from the reaction interface to the solution. When the thickness of the
13
14 rudimentary nanoporous Cu or Cu-Ag layer increases to a critical value of d_c , the temperature (T)
15
16 underneath the rudimentary nanoporous Cu or Cu-Ag layer would exceed the glass transition
17
18 temperature ($T_g=143-149$ °C) of the Mg-Cu(Ag)-Gd metallic glasses ($T>T_g$), thus reaction latent
19
20 heat-induced local glass transition occurs (Fig. 6b). The formation of the solid/liquid interface
21
22 between the rudimentary nanoporous Cu or Cu-Ag layer and the underlying supercooled liquid
23
24 layer impedes increase in the thickness of rudimentary nanoporous Cu or Cu-Ag layer, although Mg
25
26 and Gd in the rudimentary nanoporous layer and the supercooled liquid layer continue to dissolve.
27
28 Due to the bulging effect of the in situ-generated H_2 agglomerating on the solid/liquid interface, the
29
30 Cu-rich or Cu-Ag rich UF-NPF with a thickness of d_c starts to separate from the further dealloyed
31
32 supercooled liquid layer (or intermeditate nanoporous Cu or Cu-Ag), as illustrated in Fig. 6c-d.
33
34 Finally, fully dealloyed Cu or Cu-Ag UF-NPF would self-peel off from the outer surface of the
35
36 thick Mg-Cu(Ag)-Gd metallic glass ribbon (Fig. 6d).
37
38
39
40
41
42
43

44 3.3. Discussion

45
46 Besides the use of metallic glass precursor alloys with low T_g to induce a solid/liquid interface
47
48 during dealloying, we found that the introduction of HCl/ethanol solution is also crucial for the self-
49
50 peeling of flexible metallic UF-NPFs from thick Mg-Cu(Ag)-Gd metallic glass ribbons. First,
51
52 ethanol with lower thermal conductivity ($\lambda = 0.18$ W/m·K) and heat capacity ($C = 2.4$ kJ/kg·K)
53
54 compared to water is beneficial to the accumulation of latent heat, thus promoting local temperature
55
56 rise above T_g to induce local glass transition of the dealloying metallic glass precursors. Second,
57
58 ethanol instead of water can greatly decelerate the dealloying process, thus facilitating the
59
60

1 separation of intact Cu and Cu-Ag UF-NPFs from the solid/liquid interface by a mild process. Third,
2 because GdCl₃ and MgCl₂ are highly soluble (the solubility of GdCl₃ and MgCl₂ in ethanol at 298 K
3 is about ~2.4 mol kg⁻¹ and ~0.7 mol kg⁻¹, respectively) [46,47], while MgSO₄ and Gd₂(SO₄)₃ are
4 insoluble in ethanol, HCl rather than H₂SO₄ is selected as the most suitable acid for dealloying
5 (HNO₃ is also excluded because of its strong oxidability). In view that the dealloying of similar
6 Mg₆₀Cu₃₀Y₁₀ and Mg₆₅Cu₂₅Gd₁₁ metallic glass ribbons in H₂SO₄ aqueous solution just lead to the
7 formation of thick nanoporous Cu ribbons with almost unchanged thickness of the precursor
8 ribbons [18,48], we propose that the self-peeling of flexible Cu and Cu-Ag UF-NPFs from thick
9 Mg-Cu(Ag)-Gd metallic glass ribbons is attribute to an synergistic effect of HCl, ethanol, and Mg-
10 Cu(Ag)-Gd metallic glass ribbons within the dealloying system.

11 Compared to other synthesis approaches, the present dealloying approach exhibits several
12 advantages for the synthesis of flexible metallic UF-NPFs. First, the present one-step synthesis
13 procedure just simply consists of metallic glass precursors and a dilute HCl/ethanol solution, which
14 is much easier to be implemented than that of other methods with tedious multisteps. Second,
15 because it is theoretically feasible to obtain Mg-based metallic glass ribbons with arbitrary areas
16 due to their high glass forming ability [39,40], Cu and Cu-Ag UF-NPFs with huge size and/or
17 complex shapes can be prepared. For example, in the present work, a capsule shell-like Cu₃Ag UF-
18 NPF has been prepared by dealloying the outer surface of Mg₆₁Cu₂₁Ag₇Gd₁₁ metallic glass ribbon.
19 Third, the present dealloying approach is also suitable for the facile preparation of a variety of
20 multicomponent metallic UF-NPFs by simply tuning the composition of the Mg-based metallic
21 glass precursor alloys. For example, the synthesis of increasingly complex multimetallic UF-NPFs
22 containing several other alloying elements like Au, Pt, Pd, and Ir is possible by dealloying Mg-
23 Cu(Ag-Au-Pt-Pd-Ir)-Gd metallic glass precursors, since a small substitution of Cu by other
24 elements does not significantly change the T_g of the Mg-based metallic glass precursor alloys [49].

25 3.4. SERS detection of R6G

1
2 One of the most important applications of metallic UF-NPFs is as low-cost active substrates of
3
4 SERS for detecting molecules. Because R6G has been well characterized by SERS and resonance
5
6 Raman spectroscopy, here we selected R6G as our model molecule to investigate the performance
7
8 of the as-prepared Cu and Cu-Ag UF-NPFs as flexible SERS substrates. As shown in Fig. 7a, the
9
10 detection limit of R6G on Cu UF-NPFs is studied by decreasing the concentration of R6G. For
11
12 comparison purpose, the sensitivity study of R6G is also performed on a glass substrate. As can be
13
14 seen, the Raman signals of the 10^{-4} M R6G on the glass substrate are undetectable. However,
15
16 apparent intensive characteristic Raman bands of R6G at the same concentration on the Cu UF-NPF
17
18 substrates emerge, suggesting a high SERS activity of Cu UF-NPF substrates in the 10^{-4} M R6G
19
20 solution. When the R6G concentration is as low as 10^{-6} M, it still can be detected accurately,
21
22 indicating that the Cu UF-NPF substrates have a detection limit of 10^{-6} M for R6G. Although the
23
24 detection limit of the Cu UF-NPF substrates is not as good as those were made of nonporous Au
25
26 and Ag substrates [50], the detection limitation of 10^{-6} M is lower than most of the reported Cu
27
28 substrates, which only show a detectable concentration of 10^{-4} M or 10^{-5} M for R6G (Table 1) [4,51-
29
30 53]. Fig. 7b shows that the detection limits of R6G on the Cu_3Ag and CuAg UF-NPF substrates are
31
32 10^{-8} M and 10^{-11} M, respectively, and the SERS signals increase dramatically with the increase in
33
34 Ag content. The SERS improvement with the silver displacement can be explained by the fact that
35
36 silver has a stronger SERS effect than copper, due to its low absorption loss and sharp plasmon
37
38 resonance in the visible range [50]. The detection limits of the Cu_3Ag and CuAg UF-NPF substrates
39
40 are comparable to that of nanoporous Au, and also are lower than most of the Cu-Ag substrates
41
42 prepared by other methods (Table 1) [6,54-56], suggesting that the silver displaced Cu_3Ag and
43
44 CuAg UF-NPF substrates are promising cost effective flexible SERS substrates mainly containing
45
46 inexpensive copper.
47
48
49
50
51
52
53

54 55 **4. Conclusion**

56
57
58 In conclusion, we present a novel strategy to prepare flexible Cu, Cu_3Ag , and CuAg UF-NPFs
59
60 with thicknesses of ~ 200 nm by dealloying the outer surface of thick Mg-Cu(Ag)-Gd metallic glass

1
2 ribbons. The formation mechanism of such metallic UF-NPFs was investigated by analyzing the
3
4 different intermediate products in detail. It was revealed that the local reaction latent heat-induced
5
6 glass transition of the metallic glass ribbons during dealloying plays a key role in self-peeling of the
7
8 Cu, Cu₃Ag, and CuAg UF-NPFs from the outer surface of the corresponding metallic glass ribbons.
9
10 In addition, the SERS performance of the as-prepared Cu, Cu₃Ag, and CuAg UF-NPFs was
11
12 investigated. The detection limits of R6G on the Cu and CuAg UF-NPF substrates are 10⁻⁶ M and
13
14 10⁻¹¹ M, respectively, which are lower than most of the reported Cu and Cu-Ag substrates. The
15
16 present strategy not only greatly simplifies the synthesis of a variety of cost effective and flexible
17
18 metallic UF-NPFs by a simple and efficient route, but also provides a new perspective for the
19
20 application of metallic glasses.
21
22
23
24
25
26

27 **Declaration of Competing Interest**

28
29 None.
30
31
32
33

34 **Acknowledgements**

35
36 This work was supported by the National Natural Science Foundation of China (Grant No.
37
38 51671206 and Grant No. 51871056), the foundation from the Department of Education of
39
40 Guangdong Province (2018KZDXM069), and the Natural Science Foundation of Guangdong
41
42 Province (2019B030302010).
43
44
45
46
47
48

49 **References**

- 50
51 [1] A. Huang, Y. He, Y. Zhou, Y. Zhou, Y. Yang, J. Zhang, L. Luo, Q. Mao, D. Hou, J. Yang, J.
52
53 Mater. Sci. 54 (2019) 949-973.
54
55 [2] J. Zhang, C.M. Li, Chem. Soc. Rev. 41 (2012) 7016-7031.
56
57 [3] J. Kang, L. Chen, Y. Hou, C. Li, T. Fujita, X. Lang, A. Hirata, M. Chen, Adv. Energy Mater. 3
58
59 (2013) 857-863.
60

- 1
2 [4] L.-Y. Chen, J.-S. Yu, T. Fujita, M.-W. Chen, *Adv. Funct. Mater.* 19 (2009) 1221-1226.
3
4 [5] J. Wang, X. Liu, R. Li, Z. Li, X. Wang, H. Wang, Y. Wu, S. Jiang, Z. Lu, *Inorg. Chem. Front.*
5
6 7 (2020) 1127-1139.
7
8 [6] L.Y. Chen, L. Zhang, T. Fujita, M.W. Chen, *J. Phys. Chem. C* 113 (2009) 14195-14199.
9
10 [7] J. Erlebacher, M.J. Aziz, A. Karma, N. Dimitrov, K. Sieradzki, *Nature* 410 (2001) 450-453.
11
12 [8] T. Juarez, J. Biener, J. Weissmüller, A.M. Hodge, *Adv. Eng. Mater.* 19 (2017) 1700389.
13
14 [9] V. Bansal, H. Jani, J.D. Plessis, P.J. Coloe, S.K. Bhargava, *Adv. Mater.* 20 (2008) 717-723.
15
16 [10] C. Li, M. Iqbal, J. Lin, X. Luo, B. Jiang, V. Malgras, K.C.-W. Wu, J. Kim, Y. Yamauchi, *Acc.*
17
18 *Chem. Res.* 51 (2018) 1764-1773.
19
20 [11] T.T.H. Hoang, S. Ma, J.I. Gold, P.J.A. Kenis, A.A. Gewirth, *ACS Catal.* 7 (2017) 3313-3321.
21
22 [12] Z. Zhang, Y. Wang, Z. Qi, W. Zhang, J. Qin, J. Frenzel, *J. Phys. Chem. C* 113 (2009) 12629-
23
24 12636.
25
26 [13] Y.Z. Chen, X.Y. Ma, W.X. Zhang, H. Dong, G.B. Shan, Y.B. Cong, C. Li, C.L. Yang, F. Liu,
27
28 *J. Mater. Sci. Technol.* 48 (2020) 123-129.
29
30 [14] R. Li, X. Liu, R. Wu, J. Wang, Z. Li, K.C. Chan, H. Wang, Y. Wu, Z. Lu, *Adv. Mater.* 31
31
32 (2019) 1904989.
33
34 [15] X. Wang, R. Li, Z. Li, R. Xiao, X.-B. Chen, T. Zhang, *J. Mater. Chem. B.* 7 (2019) 4169-
35
36 4176.
37
38 [16] R. Li, X. Liu, H. Wang, Y. Wu, Z.P. Lu, *Corros. Sci.* 104 (2016) 227-235.
39
40 [17] D. Ma, Y. Wang, Y. Li, R.Y. Umetsu, S. Ou, K. Yubuta, W. Zhang, *J. Mater. Sci. Technol.* 36
41
42 (2020) 128-133.
43
44 [18] X. Luo, R. Li, Z. Liu, L. Huang, M. Shi, T. Xu, T. Zhang, *Mater. Lett.* 76 (2012) 96-99.
45
46 [19] Y. Ding, Y.-J. Kim, J. Erlebacher, *Adv. Mater.* 16 (2004) 1897-1900.
47
48 [20] X. Wen, L. Chang, Y. Gao, J. Han, Z. Bai, Y. Huan, M. Li, Z. Tang, X. Yan, *Inorg. Chem.*
49
50 *Front.* 5 (2018) 1207-1212.
51
52
53
54
55
56
57
58
59
60

- 1
2 [21] Y. Wang, C. He, W. Xing, F. Li, L. Tong, Z. Chen, X. Liao, M. Steinhart, *Adv. Mater.* 22
3
4 (2010) 2068-2072.
5
6 [22] M. Li, Y. Su, J. Zhao, H. Geng, J. Zhang, L. Zhang, C. Yang, Y. Zhang, *CrystEngComm* 17
7
8 (2015) 1296-1304.
9
10 [23] N.A. Luechinger, S.G. Walt, W.J. Stark, *Chem. Mater.* 22 (2010) 4980-4986.
11
12 [24] E. Wierzbicka, G.D. Sulka, *Sens. Actuators, B* 222 (2016) 270-279.
13
14 [25] S. Parida, D. Kramer, C.A. Volkert, H. Rösner, J. Erlebacher, J. Weissmüller, *Phys. Rev. Lett.*
15
16 97 (2006) 035504.
17
18 [26] Z. Li, D. Wang, B. Li, X. Lu, *J. Electrochem. Soc.* 157 (2010) K223-K226.
19
20 [27] C. Zhao, X. Wang, Z. Qi, H. Ji, Z. Zhang, *Corros. Sci.* 52 (2010) 3962-3972.
21
22 [28] S. Yang, X. Dai, B.B. Stogin, T.-S. Wong, *Proc. Natl. Acad. Sci. U.S.A.* 113 (2016) 268-273.
23
24 [29] B.-B. Xu, R. Zhang, X.-Q. Liu, H. Wang, Y.-L. Zhang, H.-B. Jiang, L. Wang, Z.-C. Ma, J.-F.
25
26 Ku, F.-S. Xiao, H.-B. Sun, *Chem. Commun.* 48 (2012) 1680-1682.
27
28 [30] X. Wang, C. Wang, L. Cheng, S.-T. Lee, Z. Liu, *J. Am. Chem. Soc.* 134 (2012) 7414-7422.
29
30 [31] M. Pohl, A. Otto, *Surf. Sci.* 406 (1998) 125-137.
31
32 [32] Y. Kalachyova, M. Erzina, P. Postnikov, V. Svorcik, O. Lyutakov, *Appl. Surf. Sci.* 458 (2018)
33
34 95-99.
35
36 [33] Z. Zuo, K. Zhu, C. Gu, Y. Wen, G. Cui, J. Qu, *Appl. Surf. Sci.* 379 (2016) 66-72.
37
38 [34] Y. Chen, F. Ge, S. Guang, Z. Cai, *J. Alloys Compd.* 726 (2017) 484-489.
39
40 [35] L.-B. Zhong, J. Yin, Y.-M. Zheng, Q. Liu, X.-X. Cheng, F.-H. Luo, *Anal. Chem.* 86 (2014)
41
42 6262-6267.
43
44 [36] D. He, B. Hu, Q.-F. Yao, K. Wang, S.-H. Yu, *ACS Nano* 3 (2009) 3993-4002.
45
46 [37] C.-L. Zhang, K.-P. Lv, H.-P. Cong, S.-H. Yu, *Small* 8 (2012) 648-653.
47
48 [38] M. Yang, L. Zhang, B. Chen, Z. Wang, C. Chen, H. Zeng, *Nanotechnology* 28 (2016) 055301.
49
50 [39] Q. Zheng, S. Cheng, J.H. Strader, E. Ma, J. Xu, *Scr. Mater.* 56 (2007) 161-164.
51
52 [40] Q. Zheng, J. Xu, E. Ma, *J. Appl. Phys.* 102 (2007) 113519.
53
54
55
56
57
58
59
60

- 1
2 [41] T.B. Massalski, Binary Alloy Phase Diagrams, American Society for Metals, Metals Park,
3
4 Ohio, 1986.
5
6 [42] B.D. Cullity, Elements of X-ray Diffraction, 2nd edition, Addison-Wesley, USA, 1978.
7
8 [43] C. Yang, B.H. Ko, S. Hwang, Z. Liu, Y. Yao, W. Luc, M. Cui, A.S. Malkani, T. Li, X. Wang,
9
10 J. Dai, B. Xu, G. Wang, D. Su, F. Jiao, L. Hu, Sci. Adv. 6 (2020) eaaz6844.
11
12 [44] C.-C. Lee, Y.-Y. Cheng, H.Y. Chang, D.-H. Chen, J. Alloys Compd. 480 (2009) 674-680.
13
14 [45] S. Yan, D. Sun, Y. Tan, X. Xing, H. Yu, Z. Wu, J. Phys. Chem. Solids 98 (2016) 107-114.
15
16 [46] L. Zeng, Z. Li, X. Wang, J. Chem. Eng. Data 61 (2016) 797-805.
17
18 [47] A. Merbach, M.N. Pitteloud, P. Jaccard, Helv. Chim. Acta 55 (1972) 44-52.
19
20 [48] Z. Deng, C. Zhang, L. Liu, Intermetallics 52 (2014) 9-14.
21
22 [49] A. Inoue, Acta Mater. 48 (2000) 279-306.
23
24 [50] B. Sharma, R.R. Frontiera, A.-I. Henry, E. Ringe, R.P. Van Duyne, Mater. Today, 15 (2012)
25
26 16-25.
27
28 [51] R. Li, G. Shi, Y. Wang, M. Wang, Y. Zhu, X. Sun, H. Xu, C. Chang, Optik 172 (2018) 49-56.
29
30 [52] G. Kartopu, M. Es-Souni1, A.V. Sapelkin, D. Dunstan, Phys. Stat. Sol. (A) 203 (2006) R82-
31
32 R84.
33
34 [53] Z. Hu, J. Wang, R. Li, C. Xu, X. Liu, Y. Wang, E. Fu, Z. Lu, Langmuir 34 (2018) 13041-
35
36 13046.
37
38 [54] Z. Jiang, Y. Tian, S. Ding, J. Wen, C. Wang, CrystEngComm. 18 (2016) 1200-1206.
39
40 [55] A.K. Pal, D.B. Mohan, J. Alloys Compd. 698 (2017) 460-468.
41
42 [56] L.H. Qian, X.Q. Yan, T. Fujita, A. Inoue, M.W. Chen, Appl. Phys. Lett. 90 (2007) 153120.
43
44
45
46
47
48
49
50
51
52
53
54
55
56
57
58
59
60

Table 1

Comparison of the detection limit of R6G between the proposed Cu, Cu₃Ag, CuAg UF-NPFs, and previously reported Cu-based SERS substrates.

SERS substrates	Prepared method	Detection limit of R6G	Reference
Cu films	Magnetron sputtering	10 ⁻⁶ M	[51]
Cu nanodot films	Electrodeposition	10 ⁻⁴ M	[52]
Nanoporous Cu	Dealloying	10 ⁻⁵ M	[4]
Nanoporous Cu foils	Hydrothermal method	10 ⁻⁶ M	[22]
Nanoporous Cu	Dealloying	10 ⁻⁵ M	[53]
Ag@Nanoporous Cu	Dealloying + displacement reaction	10 ⁻⁸ M	[6]
Cu-Ag nanowires	Displacement reaction	10 ⁻⁸ M	[54]
Cu-Ag films	Vacuum thermal evaporation	10 ⁻⁹ M	[55]
Nanoporous Cu-Ag	Dealloying	10 ⁻¹¹ M	[5]
Nanoporous Au	Dealloying	10 ⁻¹⁰ M	[56]
Cu UF-NPFs	Dealloying	10 ⁻⁶ M	This work
Cu ₃ Ag UF-NPFs	Dealloying	10 ⁻⁸ M	This work
CuAg UF-NPFs	Dealloying	10 ⁻¹¹ M	This work

Figure Captions

Fig. 1. Synthesis of Cu and Cu-Ag UF-NPFs *via* dealloying Mg-Cu(Ag)-Gd metallic glass ribbons.

(a) Photographs of a typical synthetic procedure for Cu UF-NPFs by dealloying thick $\text{Mg}_{61}\text{Cu}_{28}\text{Gd}_{11}$ metallic glass ribbon. (b) A photograph of a capsule shell-like Cu_3Ag UF-NPF by dealloying $\text{Mg}_{61}\text{Cu}_{21}\text{Ag}_7\text{Gd}_{11}$ metallic glass ribbon. (c) A photograph showing that the remaining $\text{Mg}_{61}\text{Cu}_{21}\text{Ag}_7\text{Gd}_{11}$ metallic glass ribbon can be removed by tearing off the capsule shell-like Cu_3Ag UF-NPF. (d-f) SEM images of the as-prepared Cu, Cu_3Ag , and CuAg UF-NPFs, respectively. (g-i) High-magnification SEM images of the as-prepared Cu, Cu_3Ag , and CuAg UF-NPFs, respectively.

Fig. 2. XRD patterns of the Mg-Cu(Ag)-Gd metallic glass precursors and the as-prepared Cu, Cu_3Ag , and CuAg UF-NPFs. The green and red vertical lines represent the reference diffraction peaks of pure Ag and Cu, respectively.

Fig. 3. TEM images of the ligaments in (a) Cu, (b) Cu_3Ag , and (c) CuAg UF-NPFs. High-magnification TEM images of the ligaments in (d) Cu, (e) Cu_3Ag , and (f) CuAg UF-NPFs. SAED patterns of the (g) Cu, (h) Cu_3Ag , and (i) CuAg UF-NPFs.

Fig. 4. STEM images, in a mapping mode, of typical ligaments in a Cu_3Ag UF-NPF: (a) TEM image, (b) high-angle annular dark field image (HAADF), (c) Cu distribution; and (d) Ag distribution. (e) High-magnification TEM image of the marked region in (a). (f, g) High-magnification TEM images in region A and B, respectively. STEM images of typical ligaments in a CuAg UF-NPF: (h) TEM image, (i) HAADF image, (j) Cu distribution, and (k) Ag distribution.

1
2 **Fig. 5.** Morphology of the sequential intermediates sampled at different reaction times. (a) SEM
3 image of the outer surface of the $Mg_{61}Cu_{28}Gd_{11}$ metallic glass precursor ribbon. (b) DSC curves of
4 the Mg-Cu(Ag)-Gd metallic glass precursor ribbons. (c) SEM image of the rudimentary nanoporous
5 Cu layer (layer *I*) and the local “melted” layer (layer *II*) at 3 min. (d) High-magnification SEM
6 image of the local “melted” layer at 3 min. (e) SEM image of the Cu-rich UF-NPF at 6 min. (f)
7 High-magnification SEM image of the Cu-rich UF-NPF at 6 min.
8
9
10
11
12
13
14
15
16
17

18 **Fig. 6.** Schematic illustration of the formation mechanism of the metallic UF-NPFs. (a) Formation
19 of rudimentary nanoporous Cu(Ag) on the outer surface of the metallic glass precursor ribbon. (b)
20 Glass transition ($T > T_g$) occurs within a layer between the rudimentary nanoporous Cu(Ag) and the
21 metallic glass ribbon core. (c) Separation of the Cu(Ag)-rich UF-NPF from the supercooled liquid
22 layer due to the bulging effect of in situ-generated H_2 on the solid/liquid interface. (d) Self-peeling
23 of the Cu(Ag) UF-NPF from the outer surface of the ribbon.
24
25
26
27
28
29
30
31
32
33

34 **Fig. 7.** Raman spectra of Cu and Cu-Ag UF-NPFs at different concentrations of R6G. (a) Raman
35 spectra of the Cu UF-NPF at different concentrations of R6G, together with the Raman spectra of a
36 10^{-4} M R6G ethanol solution on a glass substrate; (b) Raman spectra of the Cu_3Ag and CuAg UF-
37 NPFs at different concentrations of R6G.
38
39
40
41
42
43
44
45
46
47
48
49
50
51
52
53
54
55
56
57
58
59
60

Figure 1

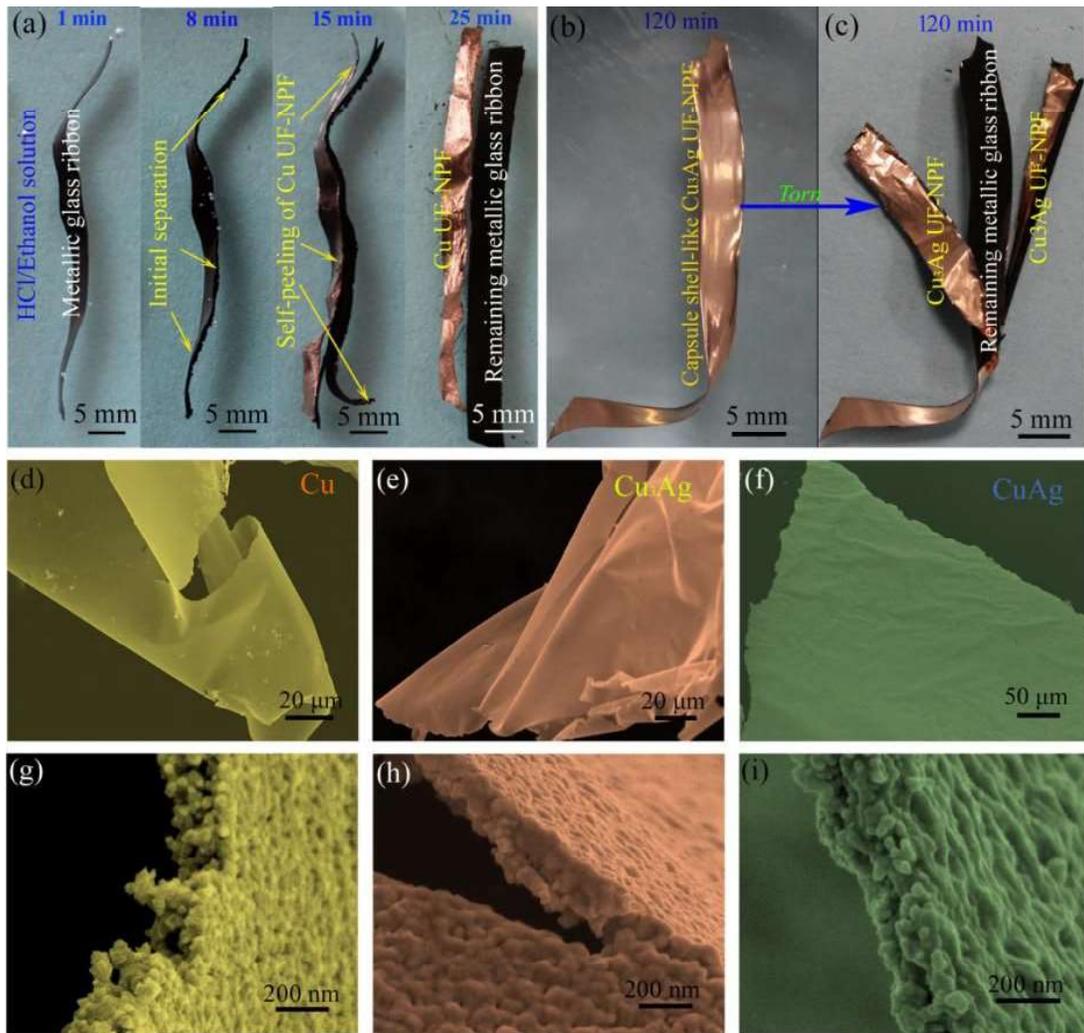


Figure 2

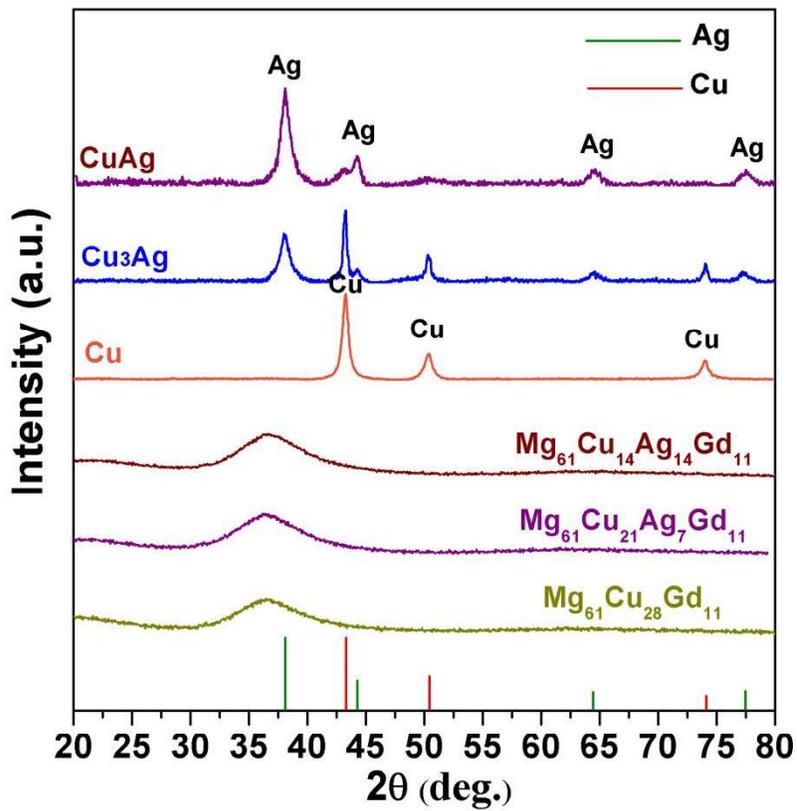


Figure 3

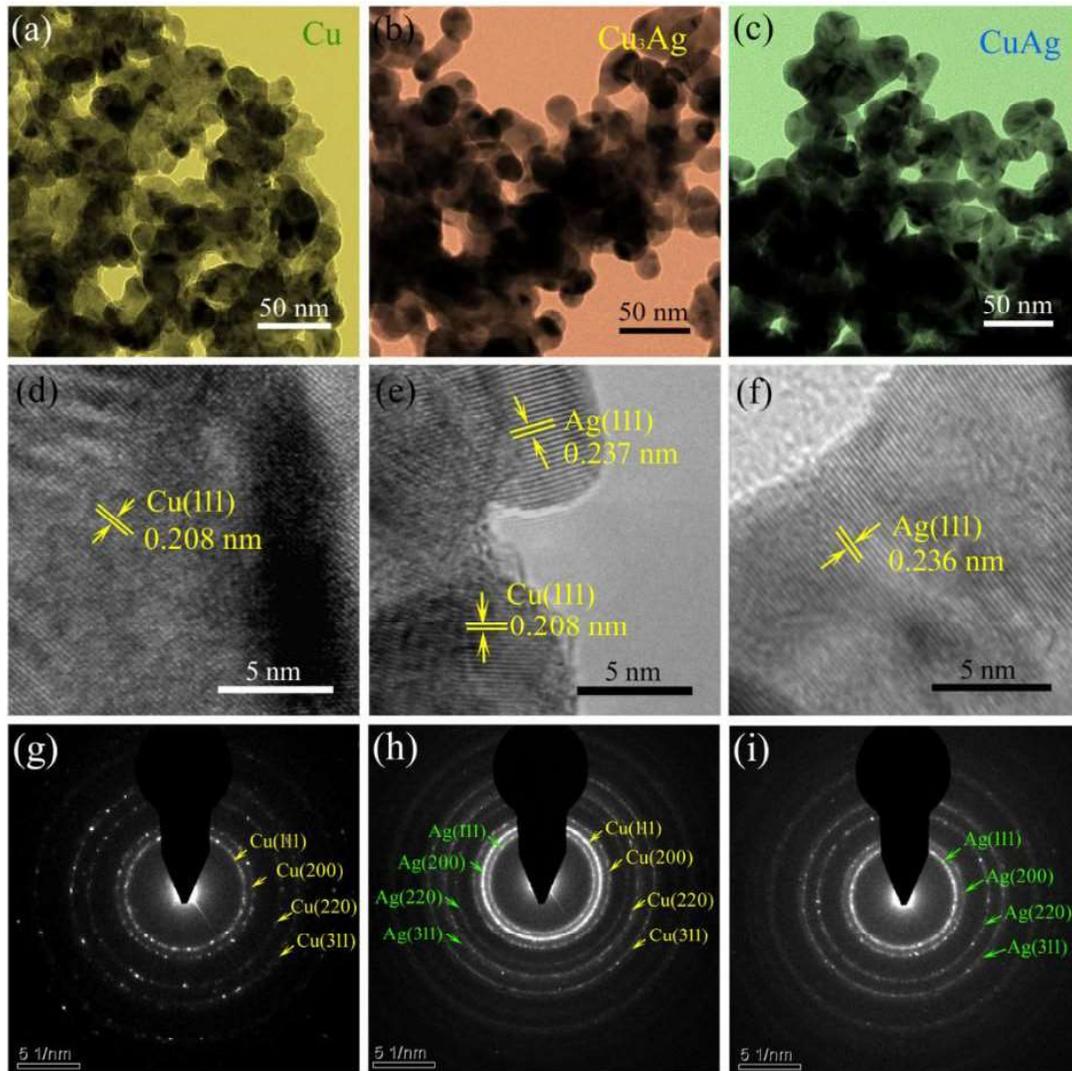
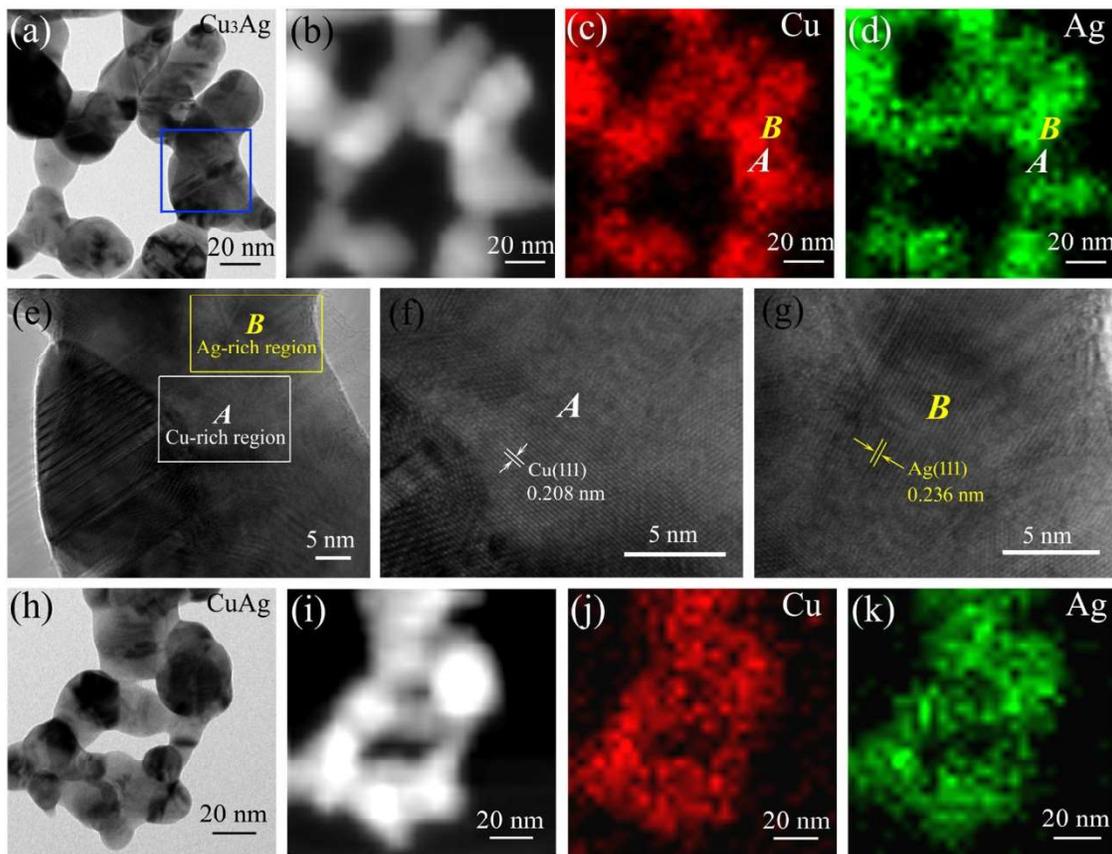


Figure 4



Only

Figure 5

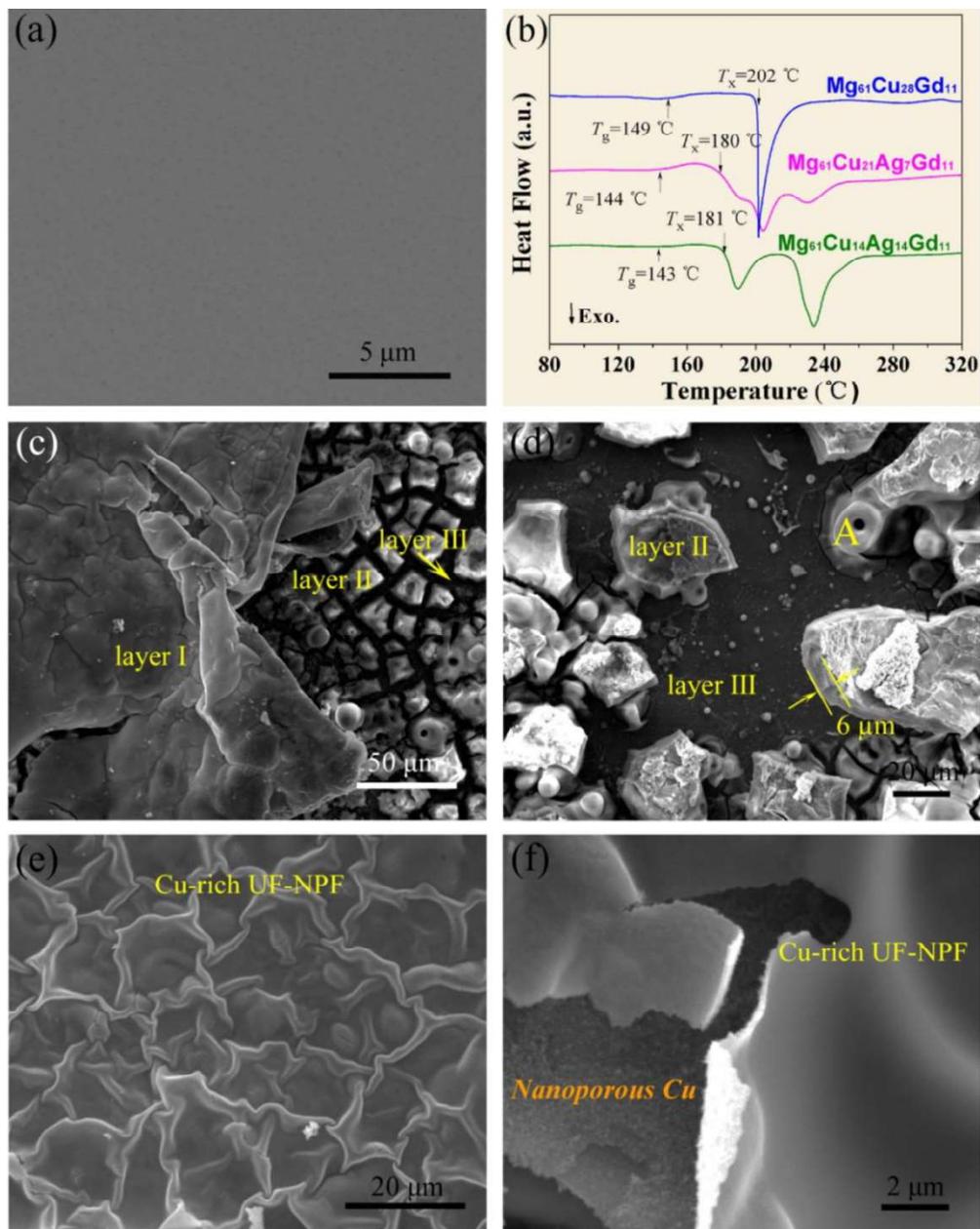


Figure 6

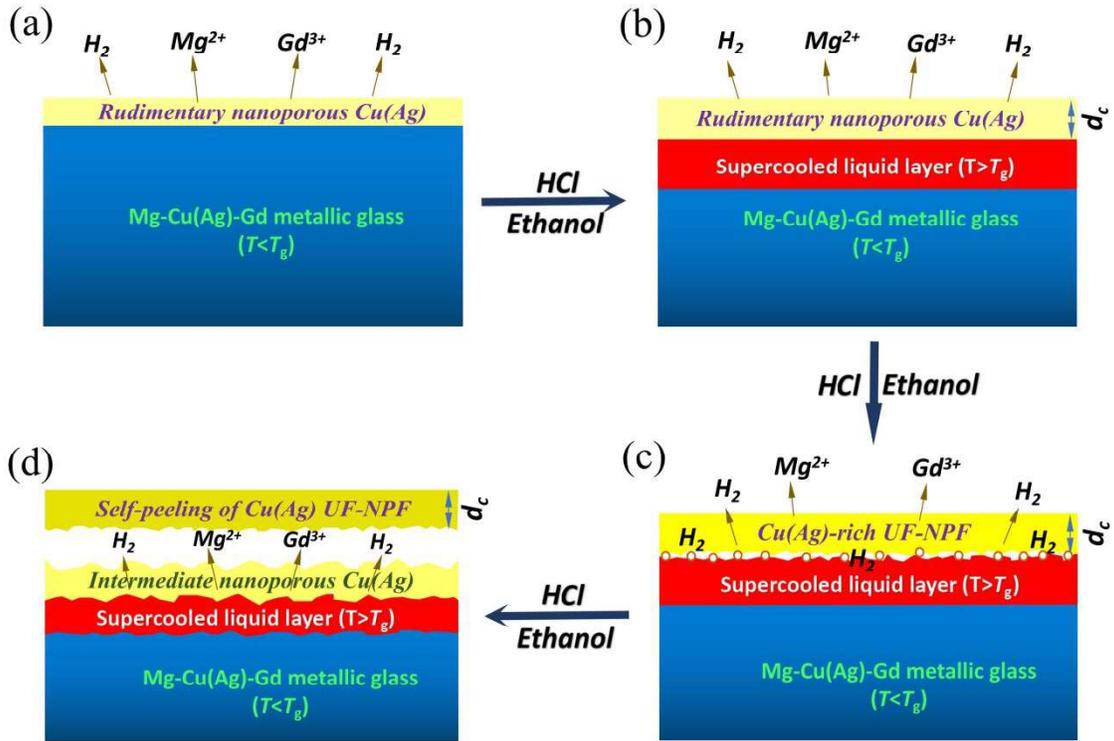


Figure 7

